Geophys. J. Int. (2002) **150,** 651–664

Constraints on upper inner-core structure from waveform inversion of core phases

R. Garcia

Laboratoire de Dynamique Terrestre et Planétaire, CNRS UMR 5562, 31400 *Toulouse, France. E-mail: garcia@pontos.cst.cnes.fr*

Accepted 2002 March 4. Received 2002 March 4; in original form 2001 May 31

SUMMARY

The determination of the inner-core boundary structure is key to understanding the mechanisms of inner-core growth, iron solidification and anisotropy formation in the inner core. A waveform inversion of a worldwide data set of *PKIKP* and *PKiKP* core phases is performed to investigate the velocity and the attenuation structure of this region. The data set is chosen to sample the top 50 km of the inner core. Two inversion methods combining time and frequency domain observations are presented. Synthetic tests are performed in order to evaluate the resolution and the confidence intervals of the model parameters. The attenuation of P waves in the uppermost inner core is poorly resolved but appears to be high ($Q < 100$). The uppermost inner-core interface is divided into two regions: a region extending from 180°W to 60°E and characterized by negative P-wave velocity perturbations ($dV/V < 0$ per cent), and a region extending from 60°E to 180°E and characterized by positive P-wave velocity perturbations ($dV/V \sim 1$ per cent). The results of the inversion do not favour the presence of transverse isotropy aligned along the spin axis of the Earth in the uppermost inner core for these two regions. However, these regions are correlated with those where large-scale variations of the inner-core anisotropy have been determined previously in the deeper inner core, 100 km beneath the inner-core boundary.

Key words: attenuation, body waves, inner core, inversion, *P* waves, waveform analysis.

1 INTRODUCTION

The Earth's inner core plays an important role in many dynamical processes of the Earth's deep interior. Body wave seismology is one of the best tools for giving us an insight into the Earth's structure. The most striking feature of inner-core P-wave velocity is a cylindrical anisotropy with a fast axis approximately parallel to the Earth's spin axis: P waves travel 2–3 per cent faster along north–south paths than in the equatorial plane (see Creager 2000, for a recent review). However, waveform and traveltime studies of core phases describe the upper 100 km of the inner core as being weakly anisotropic (Shearer 1994; Song & Helmberger 1995; Ouzounis & Creager 2001). Moreover, a disymmetry is observed between the eastern and western hemisphere: the upper 400 km of the inner core exhibits cylindrical anisotropy in the western hemisphere (180°W–40°E longitude range) but not in the eastern hemisphere (40°E–180°E) (Tanaka & Hamaguchi 1997; Creager 1999; Garcia & Souriau 2000). Some recent studies of absolute and differential traveltimes of core phases have shown, however, that anomalies ascribed to the inner-core anisotropy could be partly explained by mantle heterogeneities (Bréger *et al.* 1999, 2000).

The attenuation of the Earth's inner core has been investigated from the core phase spectra (Doornbos 1974, 1983; Niazi & Johnson 1992; Souriau & Roudil 1995; Bowers *et al.* 2000). These studies have revealed that the quality factor of P waves increases with depth from a value of 200 in the top 100 km of the inner core to 450 below. The attenuation is also possibly anisotropic, with the most attenuated paths corresponding to the paths along the spin axis of the Earth (Souriau & Romanowicz 1996).

The inner core is homogeneous at hemispherical scale, despite the hemispherical variation of the anisotropy level in the 100–400 km depth range (Creager 1999). At intermediate scale (~200 km), the heterogeneity level is low traducing the absence of strong chemical or thermal contrasts in the inner core (Garcia & Souriau 2000). However, two recent studies argue for the presence of kilometric-scale scattering in the inner core (Cormier *et al.* 1998; Vidale & Earle 2000).

The structure of the Earth's core at the inner-core boundary (ICB) has been widely investigated by seismological studies. The earliest theoretical works on body wave propagation (Richards 1973; Cormier & Richards 1977; Choy & Cormier 1983) have allowed the waveform modelling of the different core phases at all epicentral distances. By using these synthetic seismograms, the P-wave velocity and attenuation structure of the ICB region has been investigated at short periods (Cormier 1981; Choy & Cormier 1983; Cormier & Choy 1986; Cummins & Johnson 1988; Kaneshima *et al.* 1994; Huang 1996) and at long periods (Müller 1973; Häge 1983; Song & Helmberger 1992). These studies have revealed the existence of a low velocity gradient at the base of the outer core and they have allowed us to specify the *P*-wave velocity jump at the ICB, which ranges from 0.52 to 0.78 km s^{-1}. In addition, they have shown that the inner core exhibits a strong attenuation in the top 200 km beneath the ICB. The main limitations of these studies were the low number of data, investigating specific ray paths, and a trial and error inversion method based on a visual assessment of waveforms.

What is the mechanism of anisotropy formation in the inner core? How is it related to the process of iron solidification? How can we explain an hemispherical pattern of inner-core anisotropy in the 100–400 km depth range beneath the ICB? Is this hemispherical pattern associated with a structure in the uppermost inner core? The key to answering these questions is the structure of the uppermost inner core because chemical and thermal exchanges between the liquid and the solid core occur at the ICB, but also because the solidification of iron takes place at this boundary. The formation of an anisotropic velocity structure in the inner core is possibly influenced by boundary conditions at the ICB (Yoshida *et al.* 1996; Bergman 1997). In order to better constrain this region, we have developed a waveform inversion of core phases that allows us to determine simultaneously the velocity and attenuation structure in the first 50 km of the inner core. We apply this process to a selection of worldwide distributed data. The data set used is presented in the next section. Then, the computation of synthetic data and the inversion method are described. The results obtained are presented in section 5. Finally, we discuss the implication of our results for the inner-core structure and evolution.

2 DATA

2.1 Data set

Fig. 1 shows the ray paths of core phases in the Earth for the 120°–136° epicentral distance range. In this distance range, the two core phases arrive at the station with a time separation of less than 2 s and interfere on the seismogram. They follow approximately the same ray paths in the mantle and the outer core, and experience the same heterogeneities in these parts of the Earth. The hit points of *PKIKP* and *PKiKP* ray paths at the CMB are separated by less than 50 km. Only the small-scale heterogeneities in the D'' layer could have a different effect on the waveforms of the two core phases. The main difference between the ray paths is that the *PKIKP* phase passes through the inner core, whereas the *PKiKP* phase is reflected at the inner-core boundary. The turning point depth of the *PKIKP* inner-core phase is in the 0–50 km range below the inner-core boundary, sampling only the very upper part of the inner core. The 128°–136° epicentral distance range is used in this study. The lower limit is chosen in order to obtain a good resolution for the time separation between the two phases, and the upper limit is chosen to sample only the very upper part of the inner core. The data set used in this study is initially composed of 100 broad-band *PKP* vertical seismograms collected on global and temporary networks available through the NetDC e-mail service at the Geoscope or IRIS institutions. The inversion of these data is performed by comparison between data and synthetic waveforms. The computation of synthetic waveforms necessitates the estimate of the source time function of the event. For this purpose, 71 direct *P* waves in the distance range 40°–85° have been collected. These data are selected by visual inspection and resampled at a rate of 8 samples s^{-1}. Data are then filtered with a bandpass filter of corner frequencies 0.2 and 1 Hz, and analysed in this frequency band. The lower limit of the frequency band is chosen to exclude the spectral peak of the microseismic noise, and the upper limit is chosen to reduce the effect of an unmodelled signal at higher frequencies. Fig. 2 presents examples of data fitted in the 0.2–4 Hz frequency band, and shows that the high-frequency signal is not correctly fitted by the synthetic signal. The source parameters of the 43 events listed in Table 1 are extracted from the centroid moment tensor catalogue of the Harvard seismology group (Dziewonski *et al.* 1981; Ekström 1994).

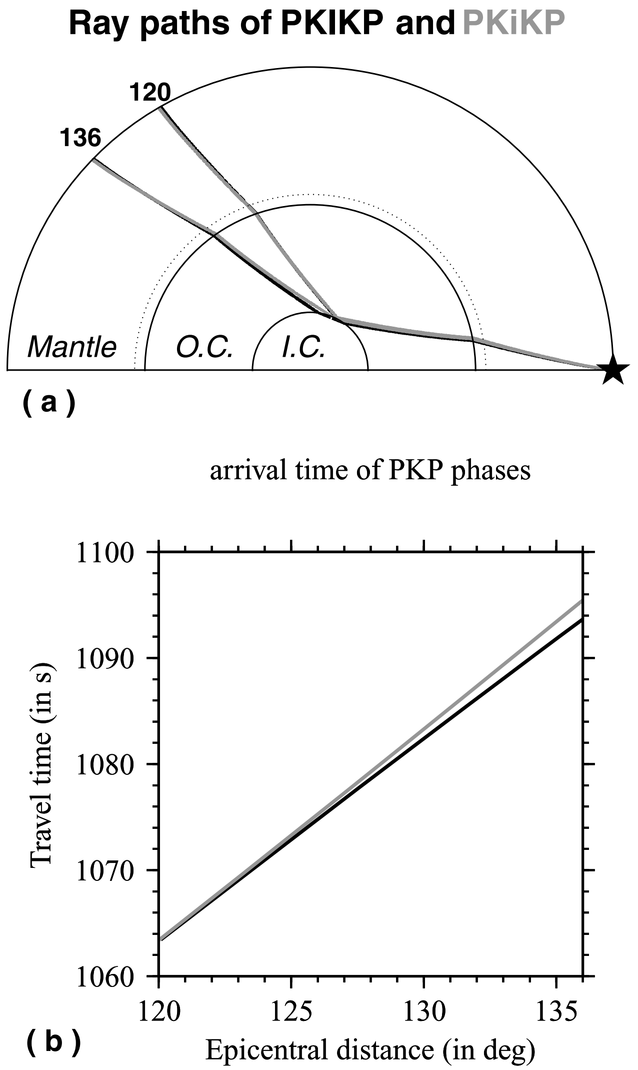

Figure 1. Ray description of the core phases. (a) Ray paths of the core-transmitted *PKIKP* wave and the core-reflected *PKiKP* wave at epicentral distances 120° and 136°. The paths of the two phases are very close to each other, except for a small path in the inner core for *PKIKP,* with a maximum turning point depth of 50 km below the ICB. (b) The traveltime curve of the core phases computed with the ak135 Earth model (Kennett *et al.* 1995) for an earthquake at 600 km depth. The maximum time lapse between the two phases is 2 s at 136° epicentral distance.

2.2 Noise and sources of error

This study uses three types of data: earthquake source parameters, *P* seismograms and *PKP* seismograms. The noise and errors contained in these three different data sets must be analysed in order to determine the selection criteria and inversion procedures that minimize their influence on the final model obtained after inversion. Earthquake mislocations have only a small effect on waveform

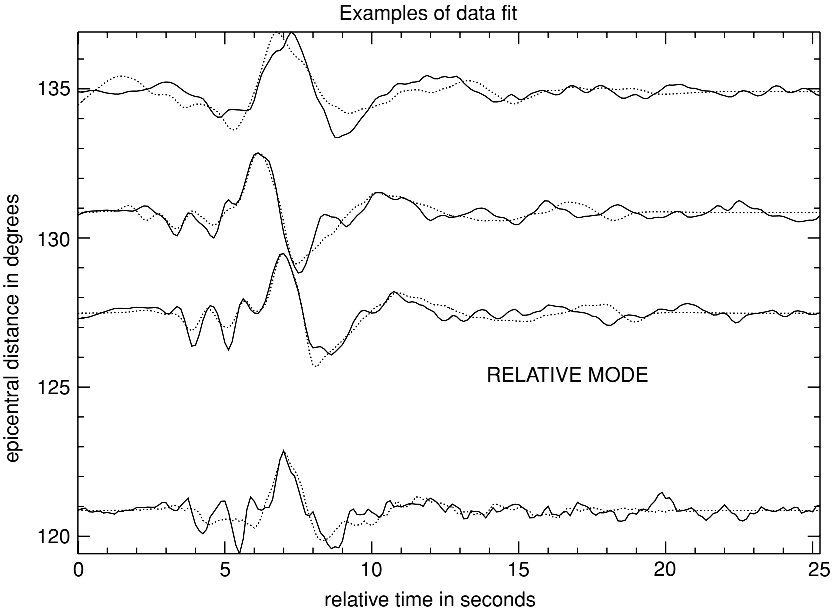

Figure 2. Example of a comparison between *PKP* data (solid line) and synthetic *PKP* waveforms (dotted line) obtained for the best model and for an earthquake at 100 km depth beneath the Santa Cruz Islands. Data and synthetic *PKP* waveforms are filtered in the 0.2–4 Hz frequency band. The shape of the main pulse is correctly fitted, but the signal for frequencies higher than 1 Hz is not correctly modelled.

studies because the traveltime of the waves are not taken into account. In contrast, the errors on the radiation pattern of the source will generate important errors on the relative amplitudes of synthetic *P* and *PKP* phases. Therefore, the amplitude of the synthetic *PKP* phase is directly subject to errors on the radiation pattern. In order to minimize the influence of heterogeneities in the source region, only earthquakes deeper than 100 km have been used. The minimum magnitude of the events is fixed to 5.8 to obtain a good signal-to-noise ratio for both *P* and *PKP* phases.

The records with large microseismic noise at the seismological station are withdrawn by visual selection of *P* and *PKP* waveforms. This selection sets an upper bound of 0.4 on the ratio of the maximum amplitude of the noise to the maximum amplitude of the signal for *P* and *PKP* data in the frequency band 0.2–1 Hz. *P* waveforms in the epicentral distance range 40°–85° are used for source time function estimates. The most important sources of error on the source time functions are the directivity effects at the source, the attenuation of the *P* wave and the crustal structure below the station. The directivity effects at the source are reduced by selecting *P* waves having a source azimuth as close as possible to the *PKP* source azimuth. The attenuation effect is reduced by selecting when possible a set of the less attenuating stations located on old continents, and inverting for a parameter correcting the differential attenuation between *P* and *PKP* ray paths. *PKP* waveforms in the 128°–136° distance range are used as inputs in the inversion process. The noise level at the station is estimated by the analysis of a time window 10 s before the *PKP* arrival. Because the stations recording *P* and *PKP* data lie on different crustal structures, the signal received at these stations is convolved by different crustal operators describing the crust response. This is an important source of discrepancies between the synthetic *PKP*, which includes the crustal response of the station recording the *P* wave, and the *PKP* seismogram, which is convolved by the crustal response below the station recording the *PKP* wave.

This analysis of noise sources has revealed two important features. One important source of noise is the difference of crustal structure between the stations recording *P* and *PKP* data. This noise could not be removed by a careful data selection or by inversion of a specific parameter. The seismological stations lying on a homogeneous crust will give the simplest signal. Secondly, the amplitude of the phases is a noisy observation because of the propagation of errors on the radiation pattern of the source and because of unmodelled effects such as focalization and defocalization of the wave front by small-scale heterogeneities or frequency-dependent attenuation in the mantle. So, we will focus our inversion on parameters independent of the amplitude of the waves.

3 COMPUTATION OF SYNTHETIC *PKP* DATA

3.1 Synthetic seismograms

The body wave data have the form

$$W = S * P(m_i) * IR, \tag{1}$$

where $W(t)$ is the waveform of the body wave recorded on the seismogram, $S(t)$ is the source time function of the event, $P(m_i)(t)$ is the propagation operator computed for the Earth model m_i and $IR(t)$ is the instrument response of the station. An empirical source time function (Cormier & Choy 1986) is estimated from a *P* waveform following

$$S\big(m_0, t_k^*\big) = W_P * P_P^{-1}(m_0) * IR_P^{-1} * AC_P\left(t_k^*\right), \tag{2}$$

where W_P is the waveform of the *P* wave, $P_P(m_0)$ is the propagation operator of the *P* wave computed for the reference model m_0, IR_P is the instrument response of the station recording the *P* wave and $AC_P(t_k^*)$ is a correction factor taking into account the attenuation structure below this station. This correction factor is written as $AC_P(t_k^*) = \exp(\pi f t_k^*)\exp(2if\ln(f/f_0)t_k^*)$ and includes corrections for the attenuation of the spectral amplitudes and the dispersion of the wave. t_k^* is the correction parameter, *f* is the frequency and f_0 is

Table 1. Characteristics of the events used in this study, extracted form the CMT catalogue of the Harvard seismology group.

Event no	Year	Julian day	hh mm ss ms	Latitude (deg)	Longitude (deg)	Depth (km)	Mw	Source length (s)
1	1989	125	18 28 40 0	−8.050	−71.490	606.0	6.4	24
2	1990	132	4 50 9 0	48.940	141.380	612.5	6.4	30
3	1992	229	10 23 31 0	−5.390	146.870	249.3	6.0	7
4	1993	19	14 39 26 0	38.700	133.960	461.6	6.0	8.8
5	1993	79	9 20 34 1	−56.110	−27.700	127.9	5.9	7.2
6	1993	144	23 51 22 0	−23.450	−66.880	231.9	6.2	15.4
7	1993	292	4 2 22 1	−22.120	−65.690	278.9	5.8	5.2
8	1994	144	21 13 18 1	56.000	161.570	100.2	5.9	3.8
9	1994	231	10 2 51 1	−26.720	−63.420	562.6	6.4	8.2
10	1995	90	14 1 40 1	38.160	135.110	366.5	6.0	5.6
11	1995	98	17 45 18 0	21.930	142.680	281.3	6.3	6.4
12	1995	175	6 58 6 1	−3.830	153.930	386.9	6.2	12
13	1995	188	21 15 18 0	33.890	137.110	348.4	5.8	4.4
14	1995	226	4 37 17 0	−4.900	151.800	140.4	6.3	11.4
15	1995	231	21 43 32 1	5.220	−75.690	128.7	6.1	9
16	1995	235	7 6 2 0	18.880	145.300	599.2	6.3	16.2
17	1995	236	1 55 34 1	18.930	145.190	594.0	5.9	6.2
18	1996	161	1 12 16 0	17.360	145.980	159.6	6.0	9.2
19	1996	188	21 36 28 0	22.020	142.990	252.5	5.8	6.4
20	1996	357	14 53 27 1	43.290	138.780	244.7	6.0	8.6
21	1997	23	2 15 22 0	−22.040	−65.920	281.6	6.4	18
22	1997	123	16 46 2 1	−31.700	−179.060	119.3	6.6	14
23	1997	133	14 13 45 1	36.510	70.680	189.1	6.1	8
24	1997	245	12 13 22 1	4.000	−75.570	213.2	6.5	11
25	1997	247	4 23 37 1	−26.450	178.520	621.0	6.3	12.6
26	1997	278	18 4 30 0	−59.900	−28.920	284.5	6.0	6.8
26	1997	287	9 53 18 1	−21.940	−176.150	165.9	6.7	35.8
27	1997	319	18 59 24 1	−14.920	167.210	121.8	6.4	15.4
28	1997	332	22 53 41 1	−13.700	−68.900	600.5	6.4	10
29	1997	345	7 56 28 0	4.110	−75.840	189.5	6.0	7.4
30	1998	4	6 11 59 0	−22.310	171.080	114.3	6.4	20.6
31	1998	38	1 18 59 1	24.920	141.870	533.6	5.9	8.2
32	1998	88	19 48 16 1	−17.570	−178.850	553.7	6.5	18.6
33	1998	136	2 22 3 0	−22.270	−179.350	608.8	6.1	13
34	1998	190	14 45 40 1	−30.510	−178.710	154.5	6.2	13.6
35	1998	197	11 56 36 1	−10.910	166.090	100.3	6.4	16.2
36	1998	232	6 40 55 1	28.990	139.470	425.5	6.1	9.4
37	1999	12	2 32 25 1	26.670	140.310	459.6	5.9	4.6
38	1999	95	11 8 4 0	−5.650	149.710	149.4	6.2	26.6
39	1999	98	13 10 34 0	43.660	130.470	575.4	6.4	16.6
40	1999	103	10 38 48 1	−21.540	−175.890	172.8	6.4	12.6
41	1999	110	19 4 8 1	−31.790	−178.790	104.4	6.2	8.8
42	1999	184	5 30 10 1	26.290	140.550	433.7	6.0	5.2
43	2000	228	4 30 8 0	−31.420	−179.950	367.4	6.0	9.4

the reference frequency of the Earth's model m_0 (here $f_0 = 1$ Hz). Using this source time function, the synthetic *PKP* body wave is computed by

$$W_{PKP}\left(t_k^*, m_i\right) = S\left(m_0, t_k^*\right) * P_{PKP}(m_i) * IR_{PKP}. \qquad (3)$$

Synthetic propagation operators of *P* and *PKP* phases for each Earth model m_i are computed with the 'full wave theory' software (Cormier 1981) provided in the 'Seismological Algorithms' package (Doornbos 1988). The method is based on a uniformly asymptotic approximation of radial eigenfunctions for *P* and *SV* waves. The model is represented by 10 polynomial velocity profiles between first-order velocity discontinuities. The main advantage of this calculation is the exact computation of attenuation and wispering gallery effects owing to underside reflection of *P* waves at the ICB. The software has been partly parallelized and runs on a 12-microprocessor CRAY-SV1 computer of the CNES (Centre National d'Etudes Spatiales) in Toulouse. Each synthetic seismogram is computed in 40 s of CPU time.

3.2 Earth model

The ak135 reference earth model (Kennett *et al.* 1995) is used in a polynomial form for *P*- and *S*-wave velocities and for the density. The attenuation parameters are extracted from the PREM model (Dziewonski & Anderson 1981), except for the inner core where the quality factor is fixed at $Q = 200$ for the reference earth model denoted m_0. Synthetic tests have been performed with realistic variations of *S*-wave velocity and density contrast at the ICB. They have shown that these two parameters have only a weak influence on the waveform of core phases in the 128°–136° epicentral distance range. The *P*-wave velocity at the base of the outer core influences strongly the absolute traveltime of core phases, but if we keep the velocity contrast at the ICB constant, the waveforms remain almost unchanged (see Cummins & Johnson 1988, Fig. 9). So, only relative variations of *P*-wave velocities above and below the ICB, velocity gradients and attenuation in the inner core influence the waveform of core phases. Since we are not able to resolve the trade-off between velocities above and below the ICB by waveform modelling of core phases in this epicentral distance range, the velocity at the base of the outer core is taken from the ak135 model. The inner-core *P*-wave velocity is investigated through the parameter $\frac{dV}{V}(m_i)$ following the formula $V_{\mathrm{IC}}(m_i, r) = V_{\mathrm{IC}}(m_0, r) + \frac{dV}{V}(m_i) * V_{\mathrm{IC}}(m_0, r_{\mathrm{IC}})$, where r is the radius and r_{IC} is the radius of the inner core. The *P*-wave velocity gradient in the inner core is kept constant and the *P*-wave velocity jump at the ICB is parametrized by $\frac{dV}{V}(m_i)$ ranging from −2 to 4 per cent by 0.5 per cent steps. The inner-core attenuation is investigated through a constant quality factor below the ICB $Q(m_i)$ ranging from 50 to 900. The synthetic propagation operators presented in Fig. 3 describe the effect of the two model parameters on the waveforms. The velocity variations have a strong influence on the waveform, particularly for epicentral distances larger than 128°, but the shape of the *PKP* impulse response has a low sensitivity to the quality factor.

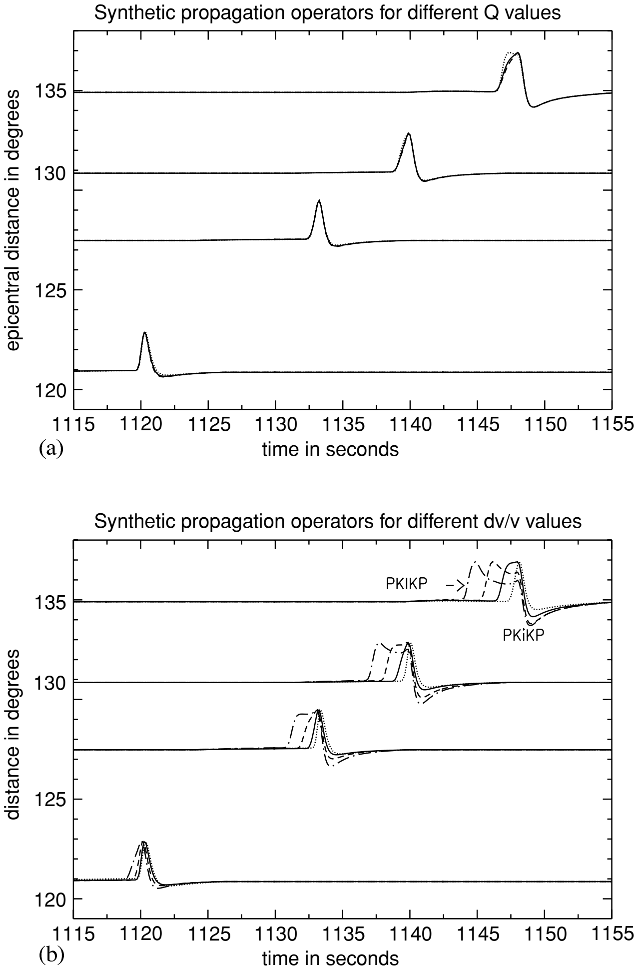

Figure 3. Synthetic impulse response of *PKP* phases to an earthquake at 100 km depth: (a) three different attenuation models with $Q = 50$ (dotted line), $Q = 100$ (solid line), $Q = 500$ (dashed line) and $dV/V =$ 0 per cent, (b) four different velocity models with $dV/V = -2$ per cent (dotted line), $dV/V = 0$ per cent (solid line), $dV/V = 2$ per cent (dashed line), $dV/V = -4$ per cent (dashed-dotted line) and $Q = 200$. Note that the velocity variations have a strong influence on the waveform, particularly at epicentral distances larger than 128°. The quality factor Q has a low influence on the pulse shape.

4 INVERSION

4.1 Inversion procedures

The *PKP* data are inverted for a parameter t^* correcting the differential attenuation between *P* and *PKP* waves, and for the uppermost inner-core *P*-wave velocity perturbation dV/V and quality factor Q, through a grid search of the best model in the parameter space. A synthetic seismogram is computed for each discrete value of t^*, dV/V and Q, aligned to *PKP* data by cross-correlation and compared by computing the misfit function between *PKP* data and the seismogram synthetic. In the previous section we saw that the amplitude of *PKP* waves is a noisy observation. So, a parameter scaling the amplitude of the waveform is inverted in the time domain, and the amplitude spectra are normalized to a reference spectral amplitude in the frequency domain. The frequency domain is usually used for estimating the attenuation of core phases (Doornbos 1974; Niazi & Johnson 1992; Souriau & Roudil 1995; Bowers *et al.* 2000). Consequently, the normalized amplitude spectrum is preferred for the estimation of the parameters t^* and Q, because these parameters influence the amplitude spectrum more strongly than the phase. However, the time domain is preferred to the frequency domain for estimating the velocity parameter dV/V, because the waveform contains the information on the time lapse between *PKIKP* and *PKiKP*, whereas the amplitude spectrum does not contain any phase information. Both time and frequency domain observations will be used in the first inversion method.

The frequency domain observation is defined as the spectral amplitude of the wave in the frequency band 0.2–1 Hz, normalized to the spectral amplitude at 0.5 Hz. The least-squares misfit function of this observation is written as

$$\text{misfit } A(d, s) = \frac{1}{N_f} \sum_{f=0.2}^{1} \frac{\{\ln[A_{\mathrm{d}}(f)/A_{\mathrm{d}}(0.5)] - \ln[A_{\mathrm{s}}(f)/A_{\mathrm{s}}(0.5)]\}^2}{\sigma^2(f)}, \tag{4}$$

where $A_{\mathrm{d}}(f)$ and $A_{\mathrm{s}}(f)$ are the spectral amplitudes of data and synthetic *PKP* phases, N_f is the number of frequencies and $\sigma^2(f)$ is the data variance. The data variance is estimated following the formula (Boatwright *et al.* 1991; Field & Jacob 1995):

$$\sigma(f) = \max\left(\frac{N_{\mathrm{d}}(f)}{A_{\mathrm{d}}(f)}, \frac{1}{2}\right), \tag{5}$$

where $N_{\mathrm{d}}(f)$ is the spectral amplitude of the microseismic noise 10 s before the *PKP* arrival. Eq. (5) constrains the data to have a maximum signal-to-noise ratio of 2. This condition gives a minimum uncertainty in order to take into account the noise arising from the different crustal structures below the *P* and *PKP* stations.

The time domain observation is defined as the waveform of the wave normalized to its maximum amplitude. A scaling parameter α is introduced in order to correct errors in the amplitude of the wave. The least-squares misfit function is written as

$$\text{misfit } W(d, s, \alpha) = \frac{1}{T_{\mathrm{W}}} \sum_{t=t_0}^{t_0+T_{\mathrm{W}}} \left(\frac{W_{\mathrm{d}}(t)}{W_{\mathrm{d}}^{\max}} - \alpha \frac{W_{\mathrm{s}}(t)}{W_{\mathrm{s}}^{\max}}\right)^2, \tag{6}$$

where $W_{\mathrm{d}}(t)$ and $W_{\mathrm{s}}(t)$ are the waveforms of the data and synthetic *PKP* phases, $W_{\mathrm{d}}^{\max}$ and $W_{\mathrm{s}}^{\max}$ their maximum amplitude, α is a scaling parameter, t_0 is the origin time 2 s before the *PKP* arrival on the synthetic seismogram and T_{W} is the duration of the window that depends on the length of the source time function of the event. In order to minimize the effect of the phase reflected on the Moho discontinuity (*PmP*), the duration of the time window is defined by $T_{\mathrm{W}} = 2 + T_{\mathrm{source}}$, if $T_{\mathrm{source}} < 10$ s, and $T_{\mathrm{W}} = 2 + 10$ s, if $T_{\mathrm{source}} \geq 10$ s, where T_{source} is the duration of the source time function. So, only the beginning of the waveform is analysed in order to avoid contamination by the *PmP* phase arriving about 11 s after the first onset. The scaling parameter α is inverted by a grid search in the range $[\frac{1}{3}; 3]$ with an accuracy of 0.01. The misfit function becomes

$$\text{misfit}\, W(d, s) = \min_{\alpha \in [\frac{1}{3};3]} \text{misfit}\, W(d, s, \alpha). \tag{7}$$

The first inversion process is divided into two steps. In a first step, the attenuation parameter t_k^* is estimated for each *P* station by the minimum value of the function

$$\text{mis}\, P(t_k^*) = \sum_{d \in \text{data}_{PKP}(P)} \min_{m_i}\left(\text{misfit}\, A\left(d, s\left(t_k^*, m_i\right)\right)\right), \tag{8}$$

where $\text{data}_{PKP}(P)$ is the *PKP* data set with the same *P* station used for the source time function estimate and $s(t_k^*, m_i)$ is the synthetic *PKP* waveform computed for the t_k^* attenuation parameter and the earth model m_i. The minimum value of mis $P(t_k^*)$ gives the best estimate t_{km}^* of the attenuation parameter for each *P* station. The *PKP* normalized spectral amplitudes are used because they are more sensitive to the effect of the attenuation than the shape of the *PKP* phase, and less influenced by the misalignment of data and synthetic waveforms during the inversion process. The attenuation parameter t_k^* is investigated in the range −1 to 0.5 s. The second step of the inversion process is the estimate of the best inner-core model m_{best} for each *PKP* data. m_{best} is obtained by minimizing the time domain misfit function misfit $W(d, s(t_{km}^*, m_i))$. In the second step of the inversion, the data are simultaneously inverted in order to statistically reduce the effects of the unmodelled signal. A best model is determined for regions of common turning points of *PKIKP* phase from the maximum variance reduction of the data set.

The second method of inversion consists in minimizing the misfit function misfit $W(d, s(t_k^*, m_i))$ for each *PKP* seismogram. It gives the best estimate of the parameters t_k^* and m_i for each *PKP* data. In this inversion, the attenuation parameter t_k^* corrects not only for attenuation along the *P*-wave path, but also partly for attenuation along the *PKP*-wave path in the mantle. However, this correction acts only on the source time function and does not change the relative attenuation of *PKIKP* and *PKiKP* phases owing to inner-core attenuation.

4.2 Synthetic inversion tests

Some synthetic tests have been performed in order to estimate the intrinsic resolution of the inner-core model parameters as a function

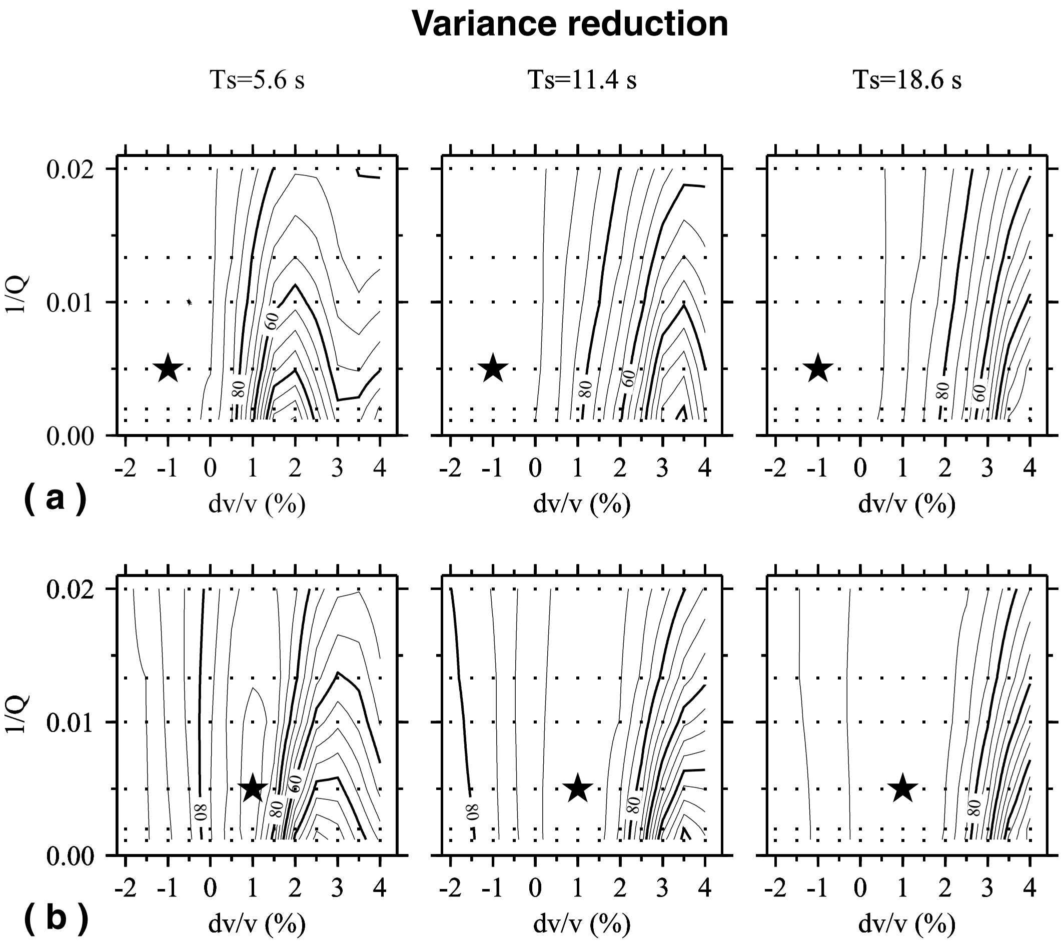

Figure 4. Contour plot of the time domain variance reduction (in per cent) as a function of the attenuation ($1/Q$) and the velocity perturbation (dV/V) for the synthetic seismograms with inner-core models $dV/V = -1$ per cent (a) and $dV/V = 1$ per cent (b) and $1/Q = 0.005$. From left to right the length of the source time function is successively 5.6, 11.4 and 18.6 s. Synthetics are computed at 130.5° epicentral distance. Contours are drawn every 5 per cent, the black star marks the maximum variance reduction (here 100 per cent), and the black dots indicate the gridpoints determined during the inversion.

of epicentral distance, inner-core velocity perturbation and duration of the source time function. Another method is developed in order to estimate the effect of microseismic noise on the inner-core model obtained after inversion. The results of these tests indicate a method of computing confidence intervals for the inner-core model parameters.

4.2.1 Intrinsic resolution of the inner-core model

As already seen in Fig. 3, the perturbations of the inner-core model change more and more the *PKP* waveforms as the epicentral distance increases, because the time separation between the two phases increases with epicentral distance, allowing a better resolution of the inner-core parameters. These synthetics also show that the attenuation parameter is poorly resolved and that the velocity perturbation is properly resolved only for epicentral distances greater than 128°. These synthetic propagation operators do not take into account the source time function of the event. In order to quantify the effect of the duration of the source time function, synthetic data are computed for three different durations of the source time function and two different inner-core models at an epicentral distance of 130.5°. These data are then inverted in the time domain, and the variance reduction as a function of the inner-core model parameters are plotted in Fig. 4. The maximum variance reduction is 100 per cent for all the plots because noise sources have not been introduced, but the shape of the variance reduction is significantly different depending on the parameters used. The intrinsic resolution of the parameters of the inner-core model increases by increasing the velocity perturbation of the initial model because the separation time between the two phases is larger. As the duration of the source time function increases, the intrinsic resolution of the parameters decreases, because long source time functions have much lower frequencies, and do not allow one to resolve the small time separation between the two phases.

4.2.2 Microseismic noise

The microseismic noise affects the *P* and *PKP* waveforms used in this study. In order to quantify the propagation of this noise in the model obtained after inversion, some synthetic inversion tests are performed by introducing noise on both *P* and *PKP* waveforms. A synthetic microseismic noise is computed by high-pass filtering a Brownian noise at 0.15 Hz. The synthetic noise presents a spectral peak at 0.15 Hz and a spectral fall-off as f^{-2} at higher frequencies.

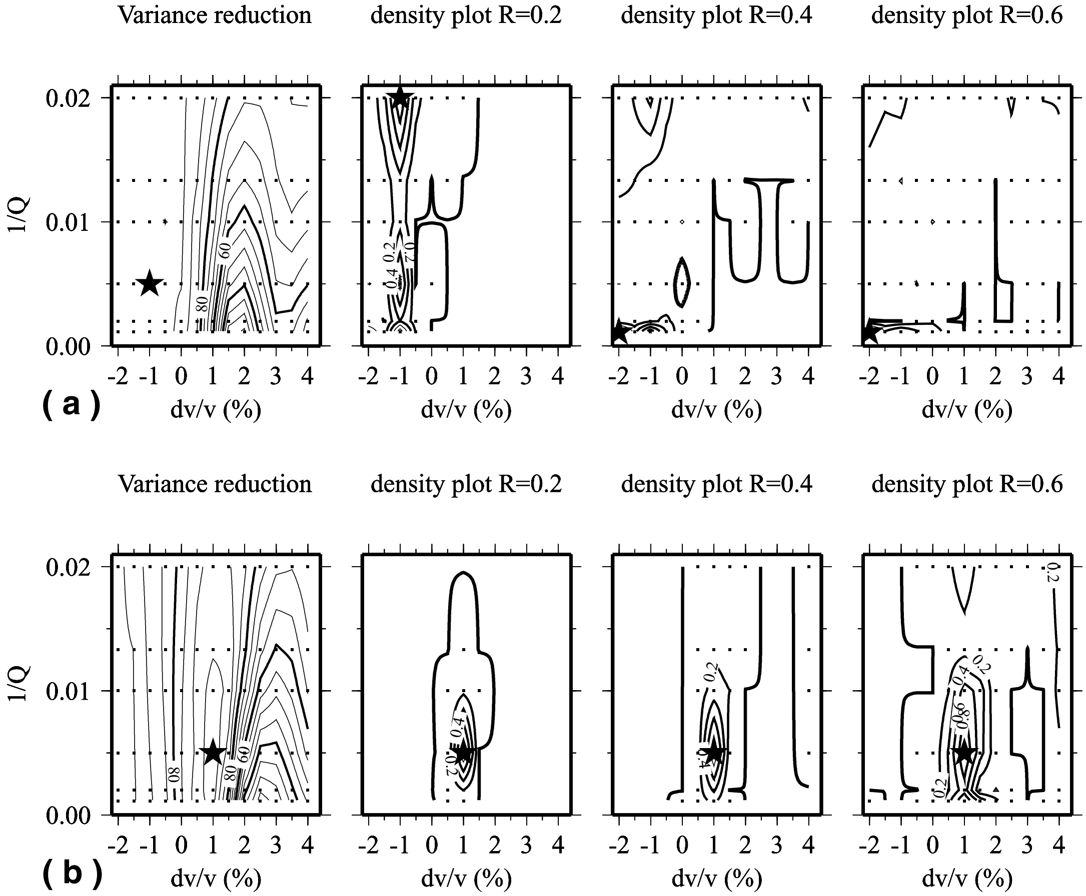

Figure 5. Synthetic inversion tests with microseismic noise added on both the source time function and the synthetic *PKP* waveform for inner-core models $dV/V = -1$ per cent (a) and $dV/V = 1$ per cent (b), and $1/Q = 0.005$ at 130.5° epicentral distance. From left to right, contour plot of the variance reduction, and contour plot of the density of the best model normalized to the peak of the distribution for the values 0.2, 0.4 and 0.6 of the ratio *R* (maximum amplitude of the noise to the maximum amplitude of the signal). Contours are drawn every 5 per cent for the variance reduction, and every 0.2 for the normalized density of the models. The black star marks the maximum variance reduction, and the peak of the density plot. The black dots indicate the gridpoints determined during the inversion for the variance reduction, and the models with non-zero density in the density plot.

The synthetic inversion test consists in adding 300 different realizations of the synthetic microseismic noise to both the source time function used to compute synthetic *PKP* seismograms, and to the *PKP* synthetic waveform used as the input data in the inversion. The distribution in the parameter space of the 300 models obtained after inversion gives an idea of the error owing to the microseismic noise for different values of the ratio R of maximal amplitude of the noise to maximal amplitude of the signal. The density of models normalized to the peak of the distribution is plotted in Fig. 5 for different inner-core models and different values of the ratio R. The variance reduction obtained for a synthetic wave without noise is recalled on the left-hand part of each panel. For the inner-core model with -1 per cent velocity perturbation, the inner-core attenuation is not resolved, even at low noise level, and the velocity perturbation is not resolved below -0.5 per cent. The density plot of the models suggest that low attenuation and negative velocity perturbations are preferred at high noise levels. For the inner-core model with 1 per cent velocity perturbation, the inner-core parameters are less influenced by noise, and the inner-core velocity perturbation is properly determined, even at high noise levels. For both inner-core initial models, the density of models has a shape that could be related to the variance reduction. Because the *P* and *PKP* data are visually selected in order to have a maximum value of 0.4 for the ratio R, the test indicates that the majority of models will be in the parameter space defined by a variance reduction larger than 90 per cent. The size of this region defines confidence intervals for the attenuation and velocity perturbation parameters. However, in this synthetic case the model without noise is known, whereas for the data, we could only access variance reduction of real data in the parameter space. So, another definition of the confidence intervals must be set because maximum variance reduction is never 100 per cent. Keeping in mind the synthetic inversion tests, we define confidence intervals for velocity $[(dV/V)_{\min}; (dV/V)_{\max}]$ and attenuation $[(1/Q)_{\min}; (1/Q)_{\max}]$ parameters by

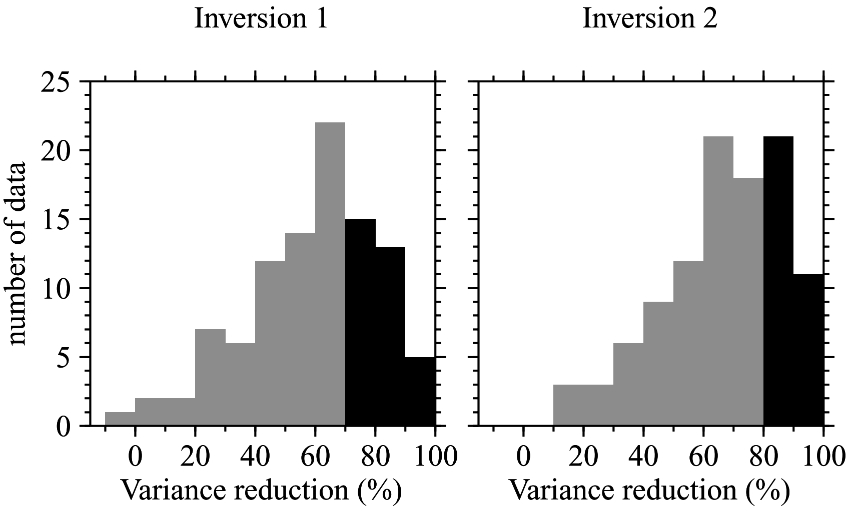

Figure 6. Histograms of the time domain variance reductions for the two inversion methods. Grey shaded areas represent the data excluded after application of the minimum variance reduction criteria.

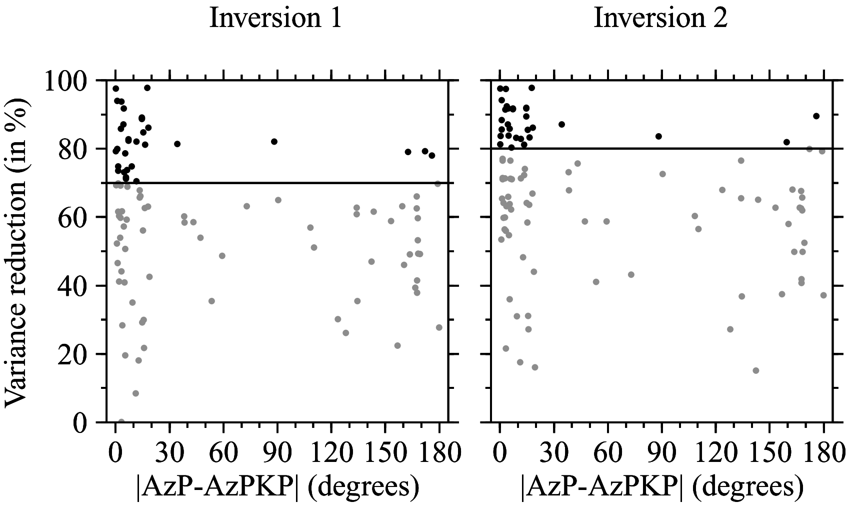

Figure 7. Time domain variance reduction (in per cent) of the best models for each data plotted as a function of the source azimuth difference between the *P* phase, which is used for a source time function estimate, and the *PKP* wave (in deg). Horizontal lines indicate the minimum variance reduction criteria, and the grey circles indicate the models that are excluded after application of these criteria.

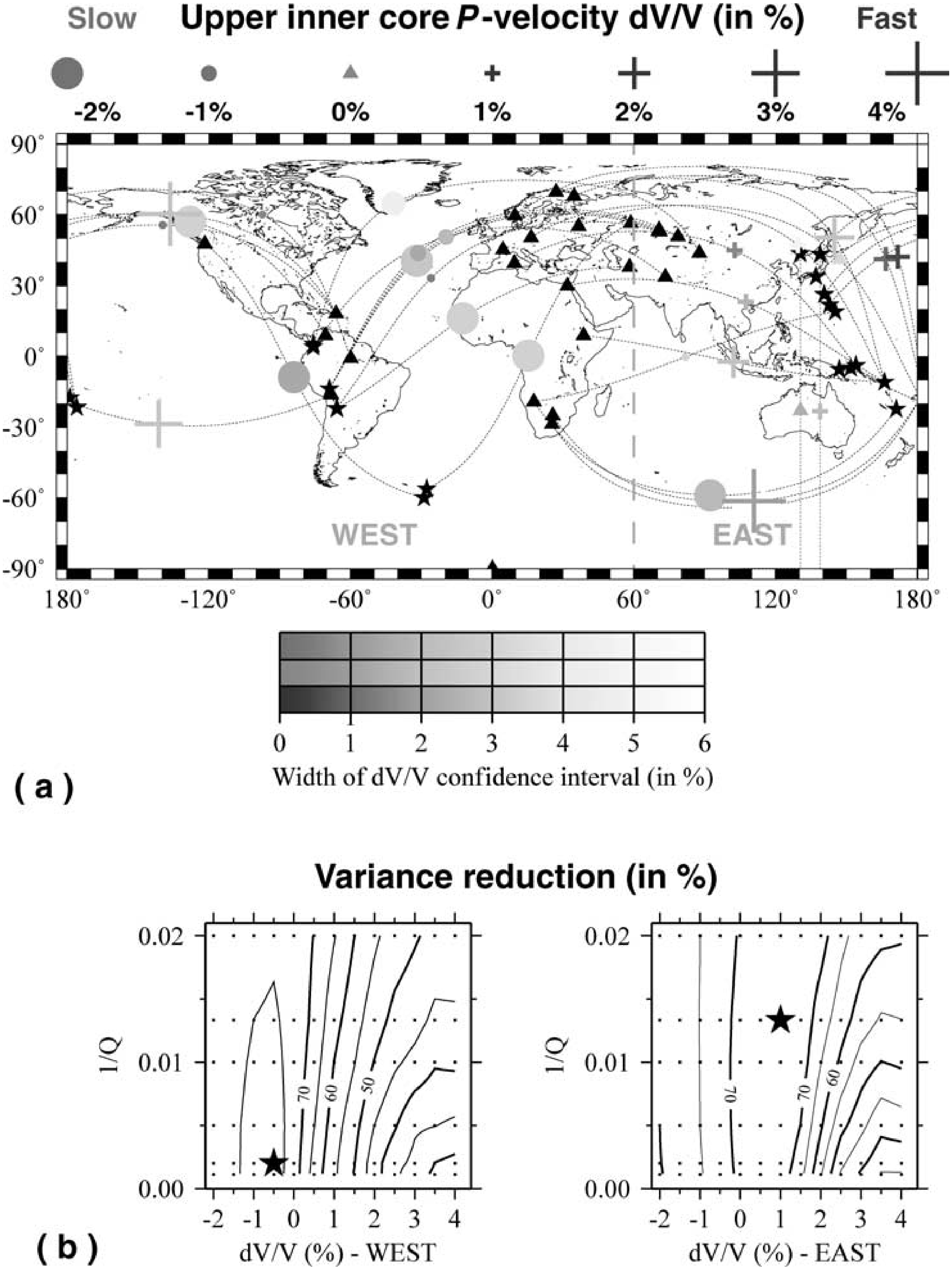

Figure 8. Uppermost inner-core model obtained by the first inversion method in the time domain. (a) The best model of upper inner-core *P*-wave velocity perturbation is represented by a symbol at the turning point of the inner-core *PKIKP* phase with a colour code indicating the width of the confidence interval. The event (black star), the seismological station (black triangle) and the ray path (dotted line) are plotted for each *PKP* data. The grey dashed line delineates two regions referenced as WEST and EAST. (b) Contour plot of the regional variance reduction (variance reduction of the whole data set of the region) for the two longitudinal regions described above. The uppermost inner-core model is investigated through the *P*-wave velocity dV/V along the *x*-axis and the inverse of the quality factor $1/Q$ along the *y*-axis. The dots give the position of the gridpoints investigated in the parameter space and the black star denotes the maximum of the variance reduction.

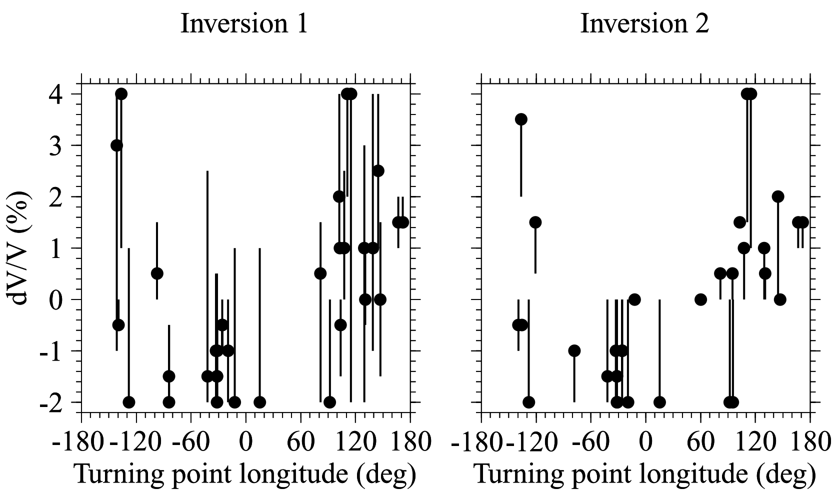

Figure 9. Velocity perturbation parameter (in per cent) as a function of the longitude in the inner core (in degrees) for the two inversion methods. Confidence intervals, calculated following formula (9), are drawn as vertical bars.

Table 2. Summary of the results obtained by the first and second inversion methods for the models filling the minimum variance reduction criteria.

Event no	*PKP* station	*P* station	IC long. (deg)	Inversion 1				Inversion 2			
				Var. red. (per cent)	$(\frac{dV}{V})$ (per cent)	$(\frac{dV}{V})_{\min}$ (per cent)	$(\frac{dV}{V})_{\max}$ (per cent)	Var. red. (per cent)	$(\frac{dV}{V})$ (per cent)	$(\frac{dV}{V})_{\min}$ (per cent)	$(\frac{dV}{V})_{\max}$ (per cent)
3	SSB	SSE	102.653	79.85	1.00	0.50	2.00	88.376	1.50	1.00	1.50
5	ARU	TAM	15.224	97.82	−2.00	−2.00	1.00	97.833	−2.00	−2.00	0.00
7	ABKT	TAM	−12.455	93.728	−2.00	−2.00	1.00	97.456	0.00	0.00	0.00
8	BDFB	PAL	−78.153	—	—	—	—	83.681	−1.00	−2.00	−1.00
11	SJG	ALE	−139.513	81.384	−0.50	−0.50	0.00	87.144	−0.50	−1.00	0.00
12	VSL	WMQ	103.804	71.651	−0.50	−1.50	0.00	—	—	—	—
13	SDV	FFC	−127.926	73.777	−2.00	−2.00	1.00	80.312	−2.00	−2.00	0.00
14	LPAZ	LZH	−141.233	79.028	3.00	−1.00	4.00	—	—	—	—
15	WMQ	KBS	−41.835	87.074	−1.50	−2.00	2.50	87.074	−1.50	−2.00	0.00
17	TSUM	PSI	81.767	91.657	0.50	−2.00	1.50	91.657	0.50	0.00	0.50
20	SPA	CTAO	138.780	79.183	1.00	−1.00	4.00	—	—	—	—
20	PTGA	FFC	−97.253	71.129	0.50	0.00	1.50	—	—	—	—
21	BRVK	PAB	−25.896	82.775	−0.50	−1.00	−0.50	91.691	−1.00	−2.00	0.00
22	KMBO	PAF	95.459	—	—	—	—	82.046	−2.00	−2.00	0.00
26	TTW	PEL	−83.989	74.896	−2.00	−2.00	−0.50	—	—	—	—
27	BDFB	HIA	−120.894	—	—	—	—	81.908	1.50	0.50	1.50
27	TSUM	PAF	95.050	—	—	—	—	82.347	0.50	0.00	0.50
28	VOS	PAB	−31.686	88.679	−1.50	−2.00	0.50	89.395	−1.50	−2.00	0.00
28	BRVK	PAB	−31.951	89.114	−1.50	−2.00	0.50	91.651	−1.50	−2.00	0.00
28	CHK	PAB	−32.761	84.718	−1.00	−2.00	0.50	85.487	−1.00	−2.00	0.00
28	KUR	PAB	−31.360	81.106	−1.00	−2.00	−0.50	83.353	−2.00	−2.00	−2.00
29	NIL	KONO	−19.635	73.044	−1.00	−2.00	0.00	83.858	−2.00	−2.00	0.00
30	TSUM	DRV	92.166	86.124	−2.00	−2.00	0.00	86.204	−2.00	−2.00	0.00
32	OBN	YSS	147.151	94.014	0.00	−1.50	1.50	94.16	0.00	0.00	0.00
32	BOSA	DRV	115.011	74.856	4.00	−2.00	4.00	83.097	4.00	1.00	4.00
32	LBTB	DRV	110.866	82.107	4.00	2.00	4.00	82.855	4.00	1.50	4.00
35	DPC	TSK	129.423	97.614	1.00	−2.00	3.00	97.614	1.00	0.00	1.00
35	FURI	COCO	102.087	70.529	2.00	1.00	4.00	—	—	—	—
35	KONO	YSS	144.910	85.897	2.50	1.00	4.00	91.48	2.00	0.00	2.00
35	KEG	KMI	107.429	79.205	1.00	0.00	2.50	81.219	1.00	0.00	1.00
37	SDV	FFC	−135.306	—	—	—	—	81.12	−0.50	−0.50	−0.50
39	SPA	WRAB	130.470	78.04	0.00	−0.50	1.00	89.588	0.50	0.00	0.50
40	LVZ	PET	166.641	79.833	1.50	1.00	2.00	85.626	1.50	1.00	1.50
40	KEV	PET	171.721	78.644	1.50	1.50	2.00	85.929	1.50	1.00	1.50
42	SJG	AAK	−136.374	82.128	4.00	1.00	4.00	83.559	3.50	2.00	3.50

$$\left(\frac{dV}{V}\right)_{\min} = \min\left[\frac{dV}{V}, \text{such as } VR\left(\frac{1}{Q}, \frac{dV}{V}\right) > (VR_{\max} - 10 \text{ per cent})\right]$$

$$\left(\frac{dV}{V}\right)_{\max} = \max\left[\frac{dV}{V}, \text{such as } VR\left(\frac{1}{Q}, \frac{dV}{V}\right) > (VR_{\max} - 10 \text{ per cent})\right] \tag{9}$$

$$\left(\frac{1}{Q}\right)_{\min} = \min\left[\frac{1}{Q}, \text{such as } VR\left(\frac{1}{Q}, \frac{dV}{V}\right) > (VR_{\max} - 10 \text{ per cent})\right]$$

$$\left(\frac{1}{Q}\right)_{\max} = \max\left[\frac{1}{Q}, \text{such as } VR\left(\frac{1}{Q}, \frac{dV}{V}\right) > (VR_{\max} - 10 \text{ per cent})\right]$$

where $VR(1/Q, dV/V)$ is the variance reduction of the data as a function of the inner-core parameters and $VR_{\max}$ is the maximum variance reduction. This formula allows us to put an error bar on the inner-core model obtained after inversion. Because only properly fitted data will approach the conditions of the test, we also operate a selection of the results by keeping only *PKP* data with $VR_{\max} >$ 70 per cent for the first inversion process, and *PKP* data with $VR_{\max} > 80$ per cent in the second inversion process. The selection is more restrictive in the second inversion method because one more free parameter (t_k^*) is available to fit the data. With this method, the variance reduction also depends on the parameter t_k^*. In this case, the confidence intervals are defined by replacing $VR(1/Q, dV/V)$ by $VR(t_{km}^*, 1/Q, dV/V)$ in eqs (9), where t_{km}^* is the value of the parameter t_k^*, which gives the maximum variance reduction over the entire set of values (t_k^*, $1/Q, dV/V$).

5 RESULTS

In this section, the results of the inversion are presented. In the first part, the performance of the inversion methods and the influence of non-linear instabilities caused by the source directivity effects are presented. In the second part, the seismic structure of the upper inner core and the results obtained for the t^* parameter are presented.

5.1 Variance reduction and non-linear instabilities

The histograms of the variance reductions obtained for the 100 *PKP* waveforms inverted in the time domain for the frequency band 0.2–1 Hz are presented in Fig. 6 for the two inversion methods. The selection of data depending on the time domain variance reduction of the best model leads to the exclusion of about two-thirds of the data set for each inversion method. The low variance reductions are caused by unmodelled effects such as the crustal structure below the stations, or a frequency-dependent attenuation in the mantle. However, they are also caused by non-linear instabilities generated by the directivity effects at the source. In order to illustrate this point, Fig. 7 presents the time domain variance reductions obtained for the two inversion methods plotted as a function of the azimuth differences at the source between the *P* wave, which is used for the source time function estimate, and the *PKP* data. For large azimuth differences, the variance reduction is mainly below the selection criterion, indicating that the source directivity effects are important, and that the selection criterion is probably a good one.

5.2 Uppermost inner-core structure

5.2.1 *Time domain inversion*

The uppermost inner-core velocity model obtained by the first inversion method is presented in Fig. 8(a). The results could be separated into two regions: a region of negative velocity perturbations

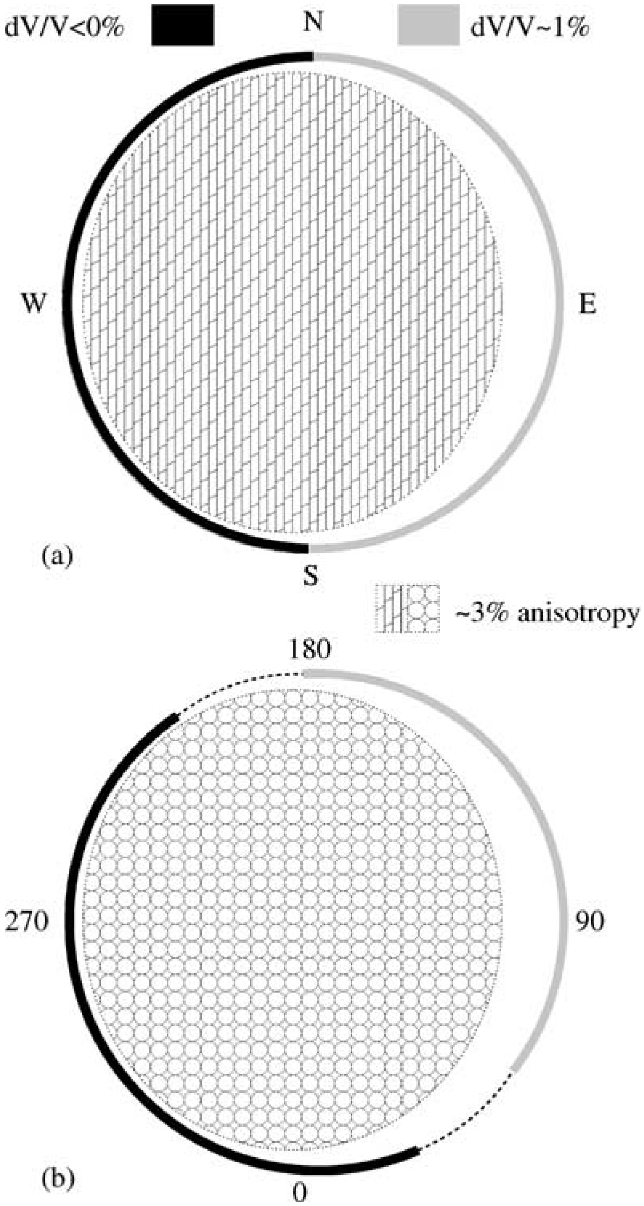

Figure 10. Meridional (a) and equatorial (b) cross-sections of the inner core showing the correlation between the asymmetrical pattern of the anisotropy variations and the upper inner-core structure. The uppermost inner-core regions with negative (positive) velocity perturbations are indicated by black (grey) areas. The central part of the inner core exhibits a cylindrical anisotropy with a fast axis aligned along the spin axis of the Earth. It is depicted by brick and circle symbols.

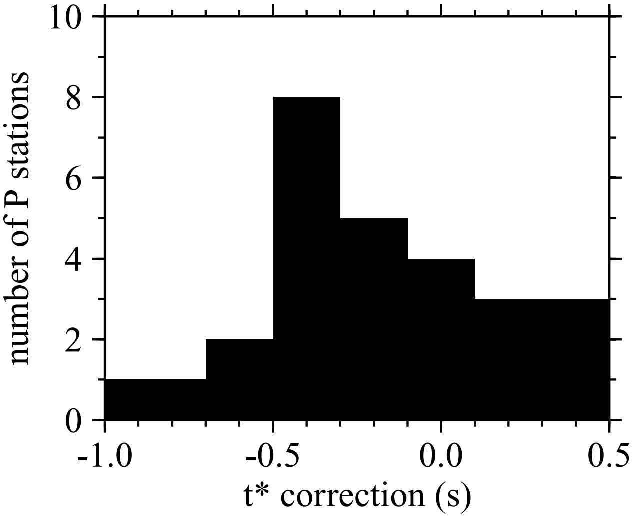

Figure 11. Histogram of the t^* values (in s) obtained for the P stations by frequency domain inversion during the first step of the first inversion method.

covering the western hemisphere (180°W–60°E), and a region of positive velocity perturbations covering a large part of the eastern hemisphere (60°E–180°E). The scatter observed in the velocity perturbations of nearby inner-core spots is caused by the large error bars of some results. The data set is separated into two longitudinal regions denoted WEST, and EAST for investigating regional variance reductions. Contour lines of the regional variance reductions in the parameter space are plotted in Fig. 8(b) for the two regions. As already mentioned in the Section 4.2.1, the quality factor Q is less constrained than the velocity perturbation, particularly for negative values of the velocity perturbation dV/V. For positive values of the velocity perturbation (EAST region), the uppermost inner-core quality factor Q has a value of 75, but it is not clearly resolved. The minima of the regional variance reductions give a velocity perturbation of -0.5 per cent for the WEST region and 1 per cent for the EAST region. Because synthetic tests have shown that negative velocity perturbations are not resolved below 0 per cent the -0.5 per cent estimate for the WEST region must be taken with caution. Moreover, the peak of the variance reduction in the EAST region is broad, indicating that the error bar is probably

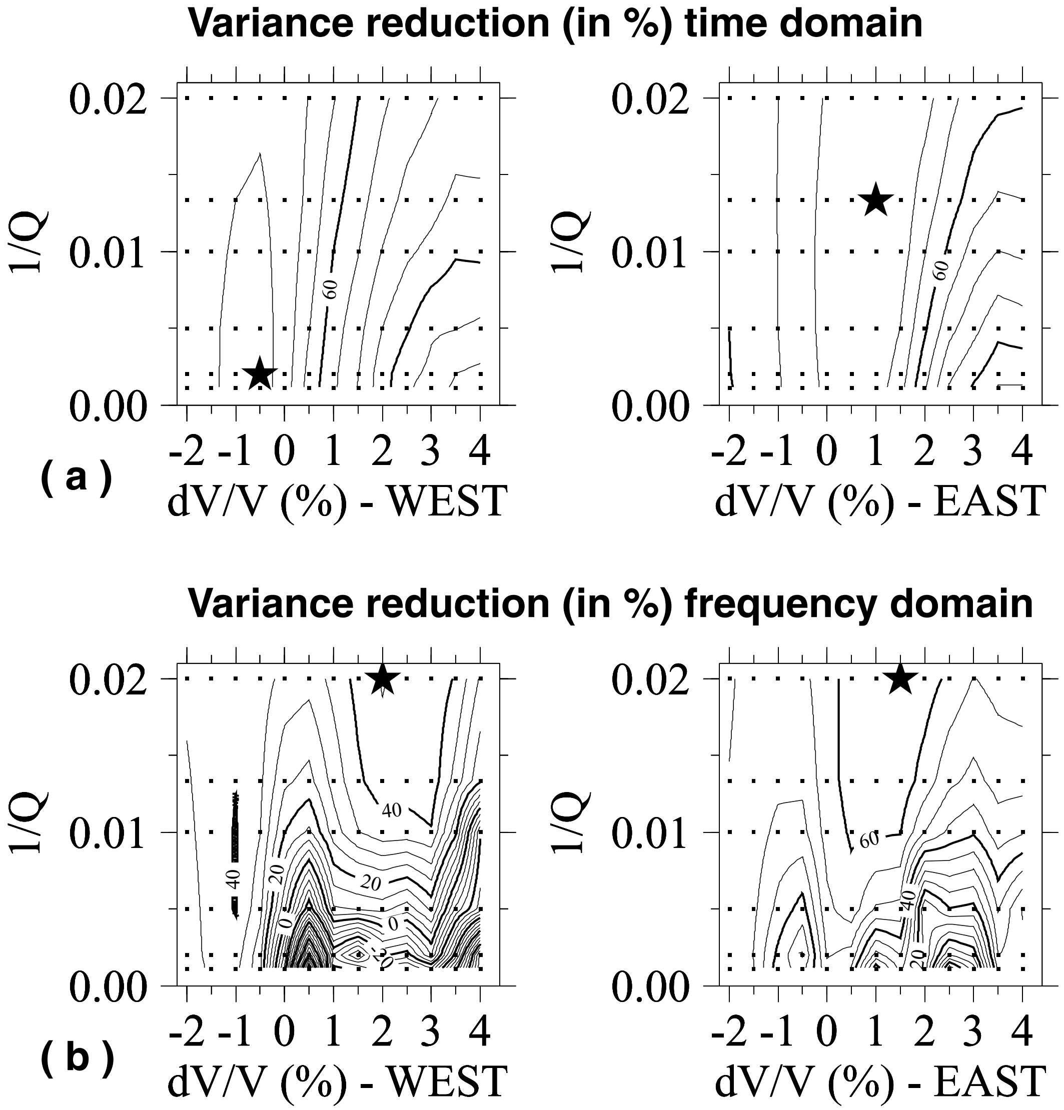

Figure 12. Time domain (a) and frequency domain (b) variance reductions as a function of the inner-core model parameters for the WEST and EAST regions. The dots give the position of the gridpoints investigated in the parameter space and the black star denotes the maximum of the variance reduction.

large. However, Fig. 9 presents the velocity perturbations obtained by the two inversion methods with their confidence intervals and clearly indicates a hemispherical pattern. The estimate of the velocity perturbations obtained by the two inversion methods are in close agreement. They are summarized in Table 2. The upper inner-core velocity perturbations presented here agree well with some recent results obtained by measurement of the differential time between *PKIKP* and *PKiKP* phases (Niu & Wen 2001). The two models present a hemispherical pattern at the top of the inner core with negative velocity perturbations in the WEST hemisphere and positive in the EAST hemisphere. The amplitudes of the regional velocity perturbations are similar, even if our estimate for the WEST region is 0.5 per cent larger. Our results appear to be noisier because the frequency band and the epicentral distance range are different, and because we use single-station information for very different events, instead of array data for selected events.

The rays used in the inversion cover a large angular range between the ray at its turning point and the Earth's spin axis, but the uppermost inner-core velocity perturbations do not appear to be correlated with this parameter, suggesting the absence of anisotropy oriented along the spin axis of the Earth in the upper part of the inner core. However, the large error bars obtained for individual velocity results do not exclude the presence of a low anisotropy level. As described in Fig. 10, the clear distinction of the uppermost inner-core structure in two different geographical areas is correlated to the distinction between an isotropic quasi-eastern hemisphere and an anisotropic quasi-western hemisphere in the 100–400 km depth range beneath the ICB (Tanaka & Hamaguchi 1997; Creager 1999; Garcia & Souriau 2000). The slow upper inner-core region corresponds approximately to the anisotropic part and the fast region to the isotropic one.

5.2.2 *Frequency domain inversion*

Frequency domain observations are used in the first step of the first inversion method to estimate the value of the t^* parameter correcting for differential attenuation between *P* and *PKP* waves. This parameter is estimated for each *P* station, but its physical significance is not obvious because it will depend on attenuation along both *P* and *PKP* ray paths. Fig. 11 presents a histogram of the results obtained for this parameter. The peak of the histogram is close to -0.4 s, traducing the fact that the attenuation of *P* waves is overpredicted by the PREM model compared with *PKP* waves. This conclusion is in agreement with the results obtained by Warren & Shearer (2000) comparing attenuation of *P* and *PP* waves in the same frequency band.

The regional variance reductions obtained in the time and frequency domains are compared in Fig. 12 for the EAST and WEST regions. Because the phase information is lost in the inversion of the logarithm of the spectral amplitude, the frequency domain inversion is less sensitive to the velocity perturbation parameter. However, the resolution of the inner-core attenuation parameter appears to be higher for the frequency domain than the time domain. So, inversion in the frequency domain gives a more precise estimate of the uppermost inner-core attenuation. These results favour a strong attenuation at the top of the inner core, with a *P*-wave quality factor in the 50–100 range.

6 CONCLUSION

A waveform inversion of a worldwide data set of core phases in the 128°–136° epicentral distance range has been performed in order to investigate the upper inner-core *P*-wave velocity and attenuation. A particular effort has been made to quantify the reliability of the upper inner-core model by using misfit functions, and by estimating the resolution of the model parameters and the confidence intervals of the results. The top 50 km of the inner core appears to be a highly attenuating medium with an average value of the *P*-wave quality factor in the 50–100 range. The uppermost inner core is separated into two regions: the first extending from 180°W to 60°E exhibits low *P* velocities ($dV/V \sim -0.5$ per cent), and the other one from 60°E to 180°E presents high *P* velocities ($dV/V \sim 1$ per cent). Moreover, the inversion results do not favour the presence of transverse isotropy aligned along the spin axis of the Earth in the top 50 km of the inner core, even if a low anisotropy level or the presence of anisotropy with another orientation cannot be excluded. The advantage of the waveform inversion is its potential to investigate small-scale structures in the inner core. However, the difficulties in correcting for the crustal structure and for the directivity of the source time function at high frequencies are two limitations of the method. Future studies must focus on these two problems in order to improve the waveform inversion method.

The uppermost inner core exhibits a hemispherical pattern with low velocities in the WEST region (180°W–60°E) and high velocities in the EAST region (60°E–180°E). If the velocity variations are caused by thermal, mineralogical or chemical heterogeneities at the top of the inner core, the hemispherical pattern could be a result of different heat flows at the ICB, possibly caused by different fluid flows at the base of the liquid core. In fact, an experimental study of outer core flows (Sumita & Olson 1999) has shown that heterogeneous heat flow conditions at the core–mantle boundary could produce an asymmetric fluid flow in the liquid core, creating an asymmetric heat flow at the ICB. The *P*-wave velocity in the top 50 km of the inner core and the anisotropic structure in the 100–400 km depth range below the ICB are approximately correlated: a large *P* velocity is correlated with the isotropic inner-core structure and a small *P* velocity with the anisotropic one. This correlation could be explained by a model of anisotropy formation by grain boundary migration in a flow owing to the isostatic adjustment generated by heterogeneous heat flow conditions at the ICB (Yoshida *et al.* 1996).

ACKNOWLEDGMENTS

I wish to thank Annie Souriau for its scientific contribution to this paper, Sébastien Chevrot for a constructive review of the manuscript and Daniel Brito for helpful discussions. I also thank Dr S. Tanaka and an anonymous reviewer for constructive reviews of the paper. This paper has been partly supported by the programme 'Intérieur de la Terre' of INSU (Institut National des Sciences de l'Univers).

REFERENCES

Bergman, M., 1997. Measurements of electric anisotropy due to solidification texturing and the implications for the Earth's inner core, *Nature,* **389,** 60–63.

Boatwright, J., Fletcher, J.B. & Fumal, T.E., 1991. A general inversion scheme for source, site, and propagation characteristics using multiply recorded sets of moderate-sized earthquakes, *Bull. seism. Soc. Am.,* **81,** 1754–1782.

Bowers, D., McCormack, D.A. & Sharrock, D.S., 2000. Observation of *PKP*(DF) and *PKP*(BC) across the United Kingdom: implication for studies of attenuation in the Earth's core, *Geophys. J. Int.,* **140,** 374–384.

Bréger, L., Romanowicz, B. & Tkalčić, H., 1999. *PKP*(BC–DF) travel time residuals and short scale heterogeneity in the deep earth, *Geophys. Res. Lett.,* **26,** 3169–3172.

Bréger, L., Tkalčić, H. & Romanowicz, B., 2000. The effect of D″ on *PKP*(AB–DF) traveltime residuals and possible implications for inner core structure, *Earth planet. Soc. Lett.,* **175,** 133–143.

Choy, G.L. & Cormier, V.F., 1983. The structure of the inner core inferred from short period and broadband GDSN data, *Geophys. J. R. astr. Soc.,* **72,** 1–21.

Cormier, V.F., 1981. Short-period *PKP* phases and the anelastic mechanism of the inner core, *Phys. Earth planet. Inter.,* **24,** 291–301.

Cormier, V.F. & Choy, G.L., 1986. A search for lateral heterogeneity in the inner core from differential traveltimes near *PKP*-D and *PKP*-C, *Geophys. Res. Lett.,* **13,** 1553–1556.

Cormier, V.F. & Richards, P.G., 1977. Full wave theory applied to a discontinuous velocity increase: the inner core boundary, *J. Geophys.,* **43,** 3–31.

Cormier, V.F., Xu, L. & Choy, G.L., 1998. Seismic attenuation of the inner core: viscoelastic or stratigraphic?, *Geophys. Res. Lett.,* **25,** 4019–4022.

Creager, K.C., 1999. Large-scale variations in inner core anisotropy, *J. geophys. Res.,* **104,** 23 127–23 139.

Creager, K.C., 2000. Inner core anisotropy and rotation, *Mineral Physics and Seismic Tomography,* AGU Monograph.

Cummins, P. & Johnson, L.R., 1988. Short-period body wave constraints on properties of the Earth's inner core boundary, *J. geophys. Res.,* **93,** 9058–9074.

Doornbos, D.J., 1974. The anelasticity of the inner core, *Geophys. J. R. astr. Soc.,* **38,** 397–415.

Doornbos, D.J., 1983. Observable effects of the seismic absorption band in the Earth, *Geophys. J. R. astr. Soc.,* **75,** 693–711.

Doornbos, D.J., 1988. *Seismological Algorithms,* Academic Press, London.

Dziewonski, A.M. & Anderson, D.L., 1981. Preliminary reference Earth model, *Phys. Earth planet. Inter.,* **25,** 297–356.

Dziewonski, A.M., Chou, T.-A. & Woodhouse, J.H., 1981. Determination of earthquake source parameters from waveform data for studies of global and regional seismicity, *J. geophys. Res.,* **86,** 2825–2852.

Ekström, G., 1994. Rapid earthquake analysis utilizes the internet, *Comp. Phys.,* **8,** 632–638.

Field, E.H. & Jacob, K.H., 1995. A comparison and test of various site-response estimation techniques, including three that are not reference-site dependent, *Bull. seism. Soc. Am.,* **85,** 1127–1143.

Garcia, R. & Souriau, A., 2000. Amplitude of the core–mantle boundary topography estimated by stochastic analysis of core phases, *Phys. Earth planet. Inter.,* **117,** 345–359.

Häge, H., 1983. Velocity constraints for the inner core inferred from long-period, *PKP* amplitudes, *Phys. Earth planet. Inter.,* **31,** 171–185.

Huang, B.-S., 1996. Investigation of the inner-outer core boundary structure from the seismograms of a deep earthquake recorded by a regional seismic array, *Geophys. Res. Lett.,* **23,** 209–212.

Kaneshima, S., Hirahara, K., Ohtaki, T. & Yoshida, Y., 1994. Seismic structure near the inner core-outer core boundary, *Geophys. Res. Lett.,* **21,** 157–160.

Kennett, B.L.N., Engdahl, E.R. & Buland, R., 1995. Constraints on seismic velocities in the Earth from traveltimes, *Geophys. J. Int.,* **122,** 108–124.

Müller, G., 1973. Amplitude studies of core phases, *J. geophys. Res.,* **78,** 3469–3490.

Niazi, M. & Johnson, L.R., 1992. Q in the inner core, *Phys. Earth planet. Inter.,* **74,** 55–62.

Niu, F. & Wen, L., 2001. Hemispherical variations in seismic velocity at the top of the Earth's inner core, *Nature,* **410,** 1081–1084.

Ouzounis, A. & Creager, K.C., 2001. Isotropy overlying anisotropy at the top of the inner core, *Geophys. Res. Lett.,* **28,** 4331–4334.

Richards, P.G., 1973. Calculation of body waves, for caustics and tunnelling in core phases, *Geophys. J. R. astr. Soc.,* **35,** 243–264.

Shearer, P.M., 1994. Constraints on inner core anisotropy from *PKP*(DF) traveltimes, *J. geophys. Res.,* **99,** 19 647–19 659.

Song, X. & Helmberger, D.V., 1992. Velocity structure near the inner core boundary from waveform modeling, *J. geophys. Res.,* **97,** 6573–6586.

Song, X. & Helmberger, D.V., 1995. Depth dependence of anisotropy of the Earth's inner core, *J. geophys. Res.,* **100,** 9805–9816.

Souriau, A. & Roudil, P., 1995. Attenuation in the uppermost inner core from broad-band GEOSCOPE *PKP* data, *Geophys. J. Int.,* **123,** 572–587.

Souriau, A. & Romanowicz, B., 1996. Anisotropy in inner core attenuation: a new type of data to constrain the nature of the solid core, *Geophys. Res. Lett.,* **23,** 1–4.

Sumita, I. & Olson, P., 1999. A laboratory model for convection in Earth's core driven by a Thermally heterogeneous mantle, *Science,* **286,** 1547–1549.

Tanaka, S. & Hamaguchi, H., 1997. Degre one heterogeneity and hemispherical variation of anisotropy in the inner core from *PKP*(BC)-*PKP*(DF) times, *J. geophys. Res.,* **102,** 2925–2938.

Vidale, J.E. & Earle, P.S., 2000. Fine-scale heterogeneity in the Earth's inner core, *Nature,* **404,** 273–275.

Warren, L.M. & Shearer, P.M., 2000. Investigating the frequency dependence of mantle *Q* by stacking *P* and *PP* spectra, *J. geophys. Res.,* **105,** 25 391–25 402.

Yoshida, Y., Sumita, I. & Kumazawa, M., 1996. Growth model of the inner core coupled with the outer core dynamics and the resulting elastic anisotropy, *Geophys. Res. Lett.,* **21,** 157–160.